Crossed-Beam Study of $Co^+(^3F_4)$+Propane: Experiment and Density Functional Theory

Sung Soo Yi,[a] Emily L. Reichert,[a] Max C. Holthausen,*[b] Wolfram Koch,[c] and James C. Weisshaar*[a]

Dedicated to Professor Paul von Ragué Schleyer on the occasion of his 70th birthday

Abstract: A pulsed beam of $Co^+(^3F_4)$ crosses a pulsed beam of C_3H_8 or C_3D_8 gas under single collision conditions at collision energies of 0.01 eV and 0.21 eV. After a variable time delay $t_{ext} = 1-8$ μs, a fast high voltage pulse extracts product ions into a field-free flight tube for mass analysis. Consistent with earlier work, we observe prompt $CoC_3H_6^+ + H_2$ elimination products in 3:1 excess over $CoC_2H_4^+ + CH_4$ products at 0.21 eV on a 2–10 μs time scale. Long-lived $CoC_3H_8^+$ complexes fragment predominantly back to $Co^+ + C_3H_8$ reactants and to H_2 elimination products on a 6–24 μs time scale. Density functional theory (B3LYP) calculations provide energies, geometries, and harmonic vibrational frequencies at key stationary points for use in a statistical rate model of the reaction. By adjusting two key multicenter transition state (MCTS) energies downward by 4–7 kcal mol^{-1}, we obtain good agreement with our decay time results and with the cross section versus collision energy of Armentrout and coworkers from 0.1–1.0 eV. B3LYP theory succeeds in finding relative energies of the MCTSs leading to CH_4 and H_2 in the proper order to explain the different product branching ratio for Co^+ (which favors H_2 over CH_4) compared with its nearest neighbors Fe^+ and Ni^+ (which favor CH_4 over H_2).

Keywords: alkanes · density functional calculations · gas-phase chemistry · reaction mechanisms · statistical rate models · transition metals

Introduction

Gas-phase transition metal cations have long been intriguing for their ability to readily break the strong CH and CC bonds of alkanes at room temperature, leading to elimination of H_2 and smaller alkane fragments.[1–3] Recently the combination of ever more incisive experimental techniques with density functional electronic structure theory (DFT),[4] which can treat quite large systems, is revealing subtle and surprising mechanistic details for these reactions.[5–8] Computational studies of the reactions of Fe^+, Co^+, and Ni^+ with small alkanes using DFT in its B3LYP formulation have examined all important stationary points on the ground state surface.[7, 9–13] They find that the rate-limiting steps involve not initial C–H or C–C bond insertion, as believed earlier, but rather passage over *multicenter transition states* (MCTSs)[14, 15] at which several bonds rearrange in concert.

The information from theory permits construction of fairly rigorous statistical rate models of the decay of long-lived [M^+(alkane)] complexes. By tuning the energies of the key MCTSs to fit a wide variety of experimental data, we can provide a critical assessment of the accuracy of transition state energies from B3LYP theory.[5–7] The key data include Armentrout's reaction cross sections versus collision energy,[16, 17] deuterium isotope effects, and our own time-resolved branching fraction measurements. We have now completed such studies of Ni^++propane[5, 6] and Ni^++*n*-butane.[5] In both cases, it is necessary to *decrease* the calculated MCTS energies by 4–7 kcal mol^{-1} to achieve good semiquantitative agreement with experiment. Very similar mechanisms describe both reactions very well. This allowed us to make educated guesses of the important mechanisms in the Co^++*n*-butane and Co^++isobutane reactions,[8] neither of which has yet been

[a] Prof. J. C. Weisshaar, Dr. S. S. Yi, E. L. Reichert
Department of Chemistry
1101 University Avenue
University of Wisconsin-Madison
Madison, WI, 53706-1396 (USA)
E-mail: weisshaar@chem.wisc.edu

[b] Dr. M. C. Holthausen
Institut für Chemie der Humboldt-Universität
Arbeitsgruppe Quantenchemie
Jägerstr. 10/11
10117 Berlin (Germany)
E-mail: mh@qc.ag-berlin.mpg.de

[c] Prof. Dr. W. Koch
Gesellschaft Deutscher Chemiker (GDCh)
Varrentrappstrasse 40–42
60486 Frankfurt am Main (Germany)

  0947-6539/00/0612-2232 $ 17.50+.50/0

studied by theory. A unified picture of M^++alkane reactions is thus emerging.

In this work we apply the same combination of techniques to the Co^++propane reaction. Significantly, we find that B3LYP theory reverses the energy order of the two key MCTSs in the case of Co^+ compared with Fe^+ and Ni^+, in accord with the experimental branching. Our crossed-beam experiment provides time-resolved branching fractions measured under carefully controlled reaction conditions for calibration of the statistical rate theory. As is well known from earlier work,[18–21] at low collision energy Co^++propane produces predominantly H_2 elimination products in preference to CH_4 elimination products. This contrasts sharply with the behavior of Fe^+ and Ni^+, its two nearest neighbors, both of which produce predominantly CH_4 in preference to H_2.[6, 16, 20–25] Once again, the modeling indicates that angular momentum conservation plays a key role in the non-exponential decay of the long-lived complexes and in subtleties of the product branching.

Experimental Section

Crossed-beam measurements

The crossed-beam apparatus and its usual operating parameters have been described previously.[6, 24, 26] In the source chamber, gas-phase cobalt atoms are produced in a laser ablation source[27] and seeded into an argon beam, which is skimmed, collimated and stripped of ions before entering the reaction chamber. The Co/Ar beam meets a second, pulsed expansion of propane gas at the center of the interaction region. The reaction begins with the arrival of an ionizing dye laser pulse at the center of this region, creating Co^+ ions in their ground electronic state. The Co^+ ions react with propane molecules in field-free space by bimolecular ion–molecule collisions. After a suitable reaction delay, a high-voltage pulse accelerates reactant and product ions toward a microchannel plate detector. The experiment runs in the single-collision regime.

A frequency-doubled dye laser beam (10 ns fwhm, 312 nm, <250 μJ per pulse) intersects the atomic beam and resonantly photoionizes Co by way of the $y^4G^0_{7/2} \leftarrow a^4F_{9/2}$ transition at 32028 cm^{-1}.[28] Absorption of two such photons creates Co^+ exclusively in the ground spin-orbit level ($^3F_4$). The two-photon energy lies 491 cm^{-1} above the ionization energy (IE) of 63565 cm^{-1}.[29] The nearest Co^+ excited state is $^3F_3$ at 951 cm^{-1} above the IE. A log–log plot of Co^+ ion yield versus laser pulse energy is linear with a slope of unity, consistent with a two-photon process whose first step is saturated. The metal ion velocity is that of the neutral beam, $(5.8 \pm 0.5) \times 10^4$ cm s^{-1}.

The packet of Co^+ (2000–7000 ions/shot) intersects the reagent beam in the extraction region of a Wiley–McLaren time-of-flight mass spectrometer.[30] Neat propane gas (Matheson $>99.9\,\%$) expands from a second 0.5 mm pulsed nozzle and is pseudo-skimmed (i.e., not differentially pumped) by a set of home-built rectangular knife edges. The mean propane beam velocity measured with a fast ion gauge is $(7.6 \pm 1.0) \times 10^4$ cm s^{-1}. We see no evidence of heavier products that might indicate the presence of a significant fraction of dimers in the propane beam. In addition, plots of product yield versus reagent backing pressure are linear from 20–120 Torr for both gases, indicating that single-collision conditions are obtained at 60 Torr and further suggesting that the beams consist primarily of monomers. Based on the work of Fenn and co-workers,[31] we estimate the internal temperature of the propane beam to be approximately 50 K.

By changing the angle between the Co^+ and reagent beams, we can vary the collision energy in coarse steps. We have conducted experiments at two such geometries, 20° and 145°. The corresponding collision energies are 0.01 ± 0.01 eV (0.2 ± 0.2 kcal mol^{-1}) and 0.21 ± 0.09 eV (4.8 ± 2.1 kcal mol^{-1}), respectively. The estimated uncertainties reflect worst-case analyses of the metal and hydrocarbon velocities, the small additional velocity imparted to the metal ions by space charge effects, and the range of angles of intersection of the two velocity vectors.

The 10 ns laser pulse initiates ion–molecule collisions at a sharply defined starting time. After a variable delay time that allows collisions to occur, reactant and product ions are extracted at time t_{ext} after the laser pulse into the time-of-flight mass spectrometer for analysis. We can obtain useful signals for extraction times in the range $0.5\ \mu s \le t_{ext} \le 8\ \mu s$. At t_{ext}, high-voltage pulses (1–1.5 kV) are applied to the ion extraction plates, accelerating reactant and product ions

Abstract in German: *Ein gepulster $Co^+(^3F_4)$-Strahl kreuzt einen gepulsten C_3H_8- bzw. C_3D_8-Strahl unter Einzelstoßbedingungen bei Kollisionsenergien von 0.01 eV und 0.21 eV. Nach einer variablen Verzögerung $t_{ext} = 1-8$ μs werden Produkt-Ionen durch einen Hochspannungspuls in ein feldfreies Flugrohr zur Massenanalyse extrahiert. In Übereinstimmung mit früheren Arbeiten wird auf einer Zeitskala von 2–10 μs 0.21 eV die spontane Bildung der Eliminierungsprodukte $CoC_3H_6^+ + H_2$ in einem 3:1 Überschuß gegenüber den Produkten $CoC_2H_4^+ + CH_4$ beobachtet. Auf einer Zeitskala von 6–24 μs fragmentieren langlebige $CoC_3H_8^+$ Komplexe hauptsächlich zurück zu den Edukten $Co^+ + C_3H_8$ sowie zu H_2-Eliminierungsprodukten. Energien, Geometrien und harmonische Schwingungsfrequenzen auf der Grundlage von Dichtefunktionalrechnungen (B3LYP) werden zur statistischen Modellierung der Reaktionskinetik verwendet. Nach Verminderung der berechneten Energien der beiden zentralen konzertierten Übergangsstrukturen um 4–7 kcal mol^{-1} ergibt sich eine gute Übereinstimmung unserer aus Abklingzeiten erhaltenen Ergebnisse mit denen von Armentrout und Mitarbeitern, die aus Messungen von Stoßquerschnitt vs. Kollisionsenergie zwischen 0.1–1.0 eV erhalten wurden. Das B3LYP-Niveau erweist sich als sehr erfolgreich bei der Beschreibung der Reihenfolge der relativen Energien der konzertierten Übergangsstrukturen, die zur Eliminierung von CH_4 und H_2 führen. Das gewählte theoretische Niveau beschreibt die unterschiedlichen Produktverteilungsverhältnisse für Co^+ (H_2-Bildung gegenüber der CH_4-Bildung bevorzugt) und seine beiden nächsten Nachbarn Fe^+ und Ni^+ (beide bevorzugen die CH_4-Eliminierung vor der von H_2) korrekt.*

towards the detector. The voltage pulses rise to 90% of their plateau values in 20 ns; the analogous rise time of the electric field in the first extraction region is about 13 ns. The mass resolution ($m/\Delta m$) is >250 for products near 100 amu. Ions are detected with a micro-channel plate detector (Galileo FTD-2003) operated at 2×10^7 gain. The detector output current drops over the 50-Ω load on a LeCroy 9400 digital oscilloscope without further amplification. We estimate detector mass discrimination effects at less than 10%.[32] Since the detector dynamic range cannot simultaneously accommodate the Co^+ ion signal and the much smaller product ion signals, a small set of electrodes mounted in the drift region is pulsed at the appropriate time to deflect Co^+ ions away from the detector.

Under single-collision conditions, total product signal should rise linearly with Co^+ number density, propane number density, and t_{ext}, which we have experimentally verified. Moreover, the reaction should be insensitive to argon backing pressure. We have run the experiment at twice and half the normal argon backing pressure of 1.7 atm with $t_{ext}=8$ μs and observe no changes in branching fractions or product yield relative to Co^+ ion signal.

It is important to distinguish clearly two different time scales. The first is the experimental time window during which the Co^+ and propane beams are "in contact" and collisions at a well defined energy may occur. This is the time between the ionizing laser pulse and the ion extraction pulse at t_{ext}. The second, which we simply call *t,* refers to the time since a long-lived complex was formed in a bimolecular collision. Because our experiment is firmly in the single-collision limit, to a good approximation we create collision complexes with a uniform distribution of initiation times over a time window of width t_{ext}. When we sample the fate of this collection of complexes at a particular real experimental time after the ionizing laser pulse, as in a time-of-flight mass spectrum, we sample complexes that have evolved over a corresponding distribution of times *t* after the initiation of the collision. This is the range of times referred to in subsequent tables of time-dependent product branching fractions.

Analysis of metastable decay by retarding potential method

Under our controlled reaction conditions, the product mass spectra reveal long-lived collision complexes. Such complexes have survived extraction intact, since they arrive at the detector at the appropriate time for the adduct ion. These complexes are metastable. They have sufficient energy to fragment either to $Co^+ + C_3H_8$ reactants or to $CoC_2H_4^+ + CH_4$ or $CoC_3H_6^+ + H_2$ exothermic elimination products. The time during which the complex accelerates in the extraction fields is about 2 μs for the typical ion extraction energy of 1380 eV. For $t_{ext}=8$ μs, complexes that survive $t=2-25$ μs after they are formed may fragment in the field-free drift region of the mass spectrometer. Even longer lived complexes will reach the detector intact.

Such metastable decay can be analyzed by applying a retarding potential in the flight tube between the extraction region and the detector, as described previously.[33–35] The retarding potential device alters arrival times in a mass-dependent fashion by first decelerating and then accelerating the ions back to their original drift velocity. In the examples presented below, we are able to distinguish long-lived complexes that survive the entire flight path intact and complexes that fragment in the first field-free region F1 (Figure 2 of reference [6]) before entering the retarding field.

Experimental Results

In Figure 1, we show product time-of-flight mass spectra taken at nominal 0.01 eV and 0.21 eV collision energy with $t_{ext}=8$ μs. At the lower collision energy, the dominant product (82 ± 2%) is the long-lived complex $CoC_3H_8^+$. We also see 2.0 ± 0.5% of the CH_4 elimination product, $CoC_2H_4^+$, and 16 ± 2% of the H_2 elimination product, $CoC_3H_6^+$. At the higher collision energy of 0.21 eV and $t_{ext}=8$ μs, we observe the same product ions but with elimination products in higher proportion. The branching fractions are 43 ± 9% $CoC_3H_8^+$, 15 ± 4% $CoC_2H_4^+$, and 42 ± 5% $CoC_3H_6^+$. The CH_4/H_2 branching ratio increases from 0.13 to 0.36 as collision energy increases. At 0.21 eV collision energy, we estimate that the reaction efficiency to form all observed products, both adducts and elimination products, is 6 ± 3% of the Langevin cross section.[36] This agrees well with the value 8% at 0.2 eV from earlier ion beam+gas experiments by Armentrout and co-workers.[37] The simple TOF-MS with $t_{ext}=8$ μs in effect samples the decay kinetics of collision complexes over a uniform distribution of times in the window $t=2-10$ μs. The resulting prompt product branching fractions including adducts are summarized for two collision energies in Table 1. In preliminary results at internal energy $E_t=0.03$ eV, CH_4 elimination accounts for 4%, H_2 elimination for 14%, and

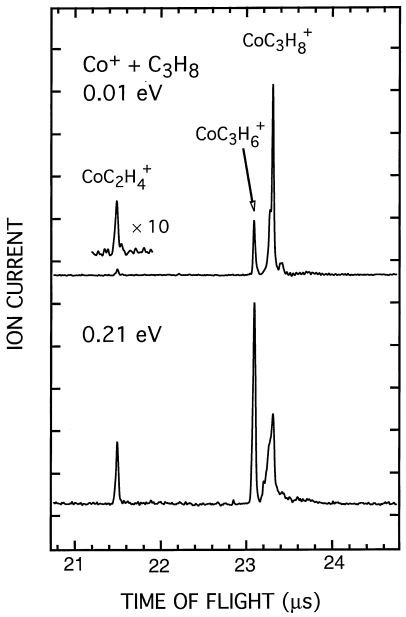

Figure 1. Product region of mass spectrum for $t_{ext}=8$ μs at collision energy 0.01 eV (top) and 0.21 eV (bottom).

0947-6539/00/0612-2234 $ 17.50+.50/0 *Chem. Eur. J.* **2000**, *6*, No. 12

Table 1. Branching fractions for Co^++C_3H_8 and Co^++C_3D_8 including long-lived complexes, $t = 2-10$ μs after initiation of collision.[a]

Reaction	E_t [eV]	$CoC_2H_4^+$ ($CoC_2D_4^+$)	$CoC_3H_6^+$ ($CoC_3D_6^+$)	$CoC_3H_8^+$ ($CoC_3D_8^+$)
Co^++C_3H_8	0.01	2 ± 0.5	16 ± 1	82 ± 1
Co^++C_3H_8	0.21	15 ± 4	42 ± 5	43 ± 9
Co^++C_3D_8	0.21	2 ± 1	5 ± 1	93 ± 2

[a] Data for $t_{ext} = 8$ μs, $U_{ext} = 1380$ eV, which places the time since initiation of Co^++C_3H_8 in the range 2–10 μs.

adducts for 82% of the products. The elimination products are behaving as if there is an energetic barrier to their formation.

The $CoC_3H_8^+$ adduct peaks in Figure 1 are clearly broadened compared to the prompt elimination product peaks. The broadening is especially evident at 0.21 eV, where the peaks have tails toward shorter TOF. At nominal 0.01 eV, a partially resolved peak toward shorter arrival time is clearly visible as well. This broadening and tailing occur in the simple TOF mass spectra because some collision complexes have fragmented in the drift region of the mass spectrometer. The strong electric field at the detector, 1300 V cm^{-1} acting over only the last 2 cm of the flight path, causes the asymmetric tailing toward shorter TOF. The lighter fragment ions suffer a larger acceleration than the intact adduct ions and thus arrive slightly earlier in time. Parents and fragments are only partially resolved by this final electric field.

The metastable decay of these long-lived $CoC_3H_8^+$ complexes was probed with the retarding field method. The purpose of the retarding field measurement is to separate all $CoC_3H_8^+$ complexes that survive extraction into two groups, those that fragment at $t \leq 25$ μs and those that do not. For $t_{ext} = 8$ μs and $E_t = 0.01$ eV, mass spectra such as those in Figure 2 sample the decay kinetics of collision complexes over a uniform distribution of times in the window $t = 6-24$ μs since initiation of a collision, as explained in detail earlier. The spectrum at retarding potential $V_r = 0$ again shows the sharp peaks due to prompt CH_4 and H_2 elimination products formed before ion extraction and the broader adduct ion peak. For an ion extraction energy $U_{ext} = 1380$ eV, a retarding potential $V_r = 400$ V can separate the $CoC_3H_8^+$ peak into very long-lived adducts (lifetime > 25 μs) and metastable fragmentation channel, Co^++C_3H_8. At the highest retarding potential shown, $V_r = 1000$ V, we see a small peak to the right of the adduct ion peak that is assigned to delayed fragmentation to $CoC_3H_6^+$ (+ H_2) formed in the drift region of the mass spectrometer. At 0.01 eV, about 48% of the long-lived complexes fragment after extraction and before exiting the retarding potential device (Table 2). Of those fragmentation products, 64% are Co^++C_3H_8, 34% are $CoC_3H_6^+$+H_2, and less than 2% are $CoC_2H_4^+$+CH_4. With $V_r \geq 1000$ V, all fragments are sufficiently retarded that the $CoC_3H_8^+$ peak becomes narrow, indicating that a substantial fraction of adduct ions have not yet fragmented when they reach the detector.

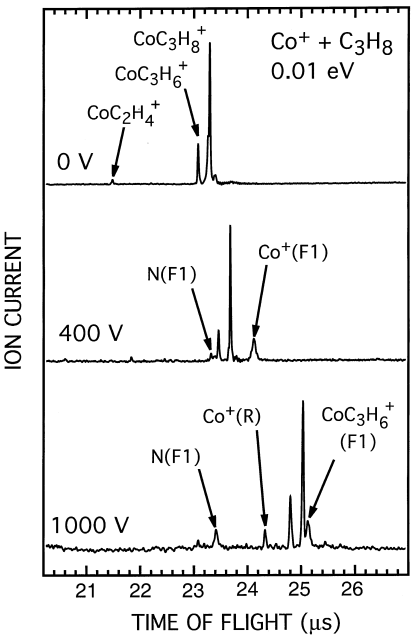

Figure 2. Product region of mass spectrum for $t_{ext} = 8$ μs at collision energy 0.01 eV versus retarding potential $V_r = 0-1000$ V as shown. N(F1) denotes neutral fragments born in first field-free region F1; Co^+(F1) and $CoC_3H_6^+$(F1) are ionic fragments born in F1. Co^+(R) are ionic fragments born in retarding region itself. See Figure 2 of reference [6] for details.

Table 2. $CoC_3H_8^+$ fragmentation pattern, $t = 6-24$ μs after collision.[a]

E_t [eV]	Fraction dissociation[a]	Fragment branching[a] Co^+	$CoC_2H_4^+$	$CoC_3H_6^+$
0.01	48 ± 5	64 ± 9	< 2[b]	34 ± 3
0.21	69 ± 12	72 ± 15	< 2[b]	27 ± 3

[a] Data for $t_{ext} = 8$ μs, $U_{ext} = 1380$ eV. Fragmentation of those ions that survive extraction as adducts but fragment before the retarding field, which places the time since initiation of Co^++C_3H_8 collisions in the range 6–24 μs. Fraction dissociated is the fraction of metastable complexes that have fragmented before reaching the detector. Fragment branching gives the product ratios for those fragments. [b] Upper bound only.

We have acquired similar retarding field mass spectra at the higher collision energy of 0.21 eV. They are qualitatively the same as the 0.01 eV spectra. In particular, the fraction of long-lived complexes returning back to Co^++C_3H_8 increases from 48% to 69% at the higher energy. Branching fractions from this "delayed" fragmentation are summarized for the two collision energies in Table 2.

For Co^++C_3D_8 at 0.21 eV, the average lifetime of adducts is substantially longer. The fraction of adducts in the simple TOF-MS increases from 43 ± 9% to 93 ± 2% upon deuteration. The prompt product branching fractions for [D_8]propane with $t_{ext} = 8$ μs are 2 ± 1% CD_4, 5 ± 1% D_2, and 93 ± 2% adducts. For both [H_8]propane and [D_8]propane, hydrogen elimination is favored over methane elimination by about a factor of 3. These branching fractions are included in Table 1. Preliminary retarding potential measurements for Co^++[D_8]-propane indicate that $Co^+(C_3D_8)$ complexes mostly return back to reactants.

We can compare this new data with previous experimental results.[19–21, 37–42] Table 3 presents the branching ratio between CH_4 and H_2 elimination products from our experiment with that observed in earlier work using a variety of techniques. In contrast to the behavior of Ni^++C_3H_8, the branching ratio is quite sensitive to collision energy or other experimental

Table 3. Comparison of elimination product branching fractions.

E_t [eV]	Technique[a]	$CoC_2H_4^+ + CH_4$	$CoC_3H_6^+ + H_2$	Ref.
0.01	CB[c]	11	89	this work
0.21	CB[c]	26	74	this work
≈1	IB + G	41	59	[38], [39]
≈0.5	IB + G	25	75	[40]
<0.2	IB + G	19	81	[37]
<0.1	IB + G	33	67	[21]
0.05	IB + G	23	73	[41]
TE[b]	ICR	31	69	[20]
TE	FR	24	76	[42]
TE	TMS	4	96	[41]
TE	TMS[d]	18	82	[18]
TE	TMS[e]	53	47	[18]

[a] CB = crossed beams; IB + G = ion beam plus gas cell; ICR = ion cyclotron resonance; FR = flow reactor at 0.75 Torr of He buffer; TMS = tandem mass spectrometry. [b] Thermal energy distributions near 300 K. [c] Ground state $Co^+(a^3F, 3d^8)$ created by resonant two-photon ionization. [d] Ground state $Co^+(a^3F, 3d^8)$ selected by ion chromatography. [e] Excited state $Co^+(a^5F, b^3F, 4s3d^7)$ selected by ion chromatography.

variables. This sensitivity might be partly due to the differences in internal electronic and vibrational energy of $Co^+ + C_3H_8$ reactants. As mentioned earlier, the resonant two-photon ionization process employed in our experiment creates the lower energy $^3F_4$ spin-orbit level of Co^+ exclusively. van Koppen et al.[18] measured state-specific branching ratios at thermal energy (≈0.04 eV) using ion chromatography and reported CH_4/H_2 branching ratio of 18/82 for ground state Co^+ (a^3F) and 53/47 for the Co^+ (a^5F, b^3F). Their branching ratio for ground state Co^+ lies between our a^3F-state-specific branching ratios of 11/89 at nominal 0.01 eV and 26/74 at 0.21 eV.

Some of the early studies mention detection of the long-lived collision complexes that form the bulk of the products observed in this work. Tolbert and Beauchamp[43] reported 39% adduct ions at $E_t = 0.5$ eV when colliding a Co^+ beam with C_3H_8 gas in a collision cell at 1.5 mTorr. Tonkyn, Ronan, and Weisshaar[42] performed their work in a fast flow reactor under multicollision conditions at 0.75 Torr of He with a 300 K Boltzmann distribution of collision energies. They found 95% intact $CoC_3H_8^+$ collision complexes, quite similar to our $t = 2-10$ μs branching results at 0.01 eV (Table 1). On the basis of simple third-body stabilization kinetics with the strong collision assumption, they deduced that the metastable $CoC_3H_8^+$ collision complexes lived at least 0.6 μs. In an ion beam+collision cell experiment, Armentrout and co-workers[41] estimated the lifetime of collision complexes formed at collision energy $E_t = 0.05$ eV from the increase in $CoC_3H_8^+$ signal with propane pressure in the cell. From a Stern–Volmer model they obtained a lifetime of 0.45 μs. In the direct complex decay measurements presented here, we observe elimination products on a sub-μs time scale but also on much longer time scales. The Stern–Volmer models did not account for the distribution of time scales arising from the angular momentum effects modeled in detail below.

Recently, van Koppen et al.[41] measured the kinetic energy release distributions (KERDs) of the metastable decay products from $CoC_3H_8^+$ parents. The $CoC_3H_8^+$ parent ions are gently extracted from an electron impact ionization source of Co^+ containing 10^{-3} Torr C_3H_8 at 300 K. They have spent 0–50 μs in the source region and an additional 6–14 μs prior to fragmentation in the second field-free region of a tandem mass spectrometer.[44] Thus the range of times since complex formation is roughly 6–64 μs. Analysis of the fragments from nascent complexes reveals 32% Co^+, 3% $CoC_2H_4^+$, and 65% $CoC_3H_6^+$. This is a much higher yield of elimination fragments than we observe for $t = 6-24$ μs at either collision energy (Table 2). Some of van Koppen's complexes likely suffer one or two stabilizing collisions in the source prior to extraction into high vacuum, which would discriminate against dissociation back to reactants.

Electronic Structure Calculations

For the C–C and C–H activation pathways in the $Co^+ + C_3H_8$ system we found a mechanism[45] (cf. Scheme 1) fully in line with earlier experience with $Co^+ + C_2H_6$, $Fe^+ + C_2H_6$ and C_3H_8,

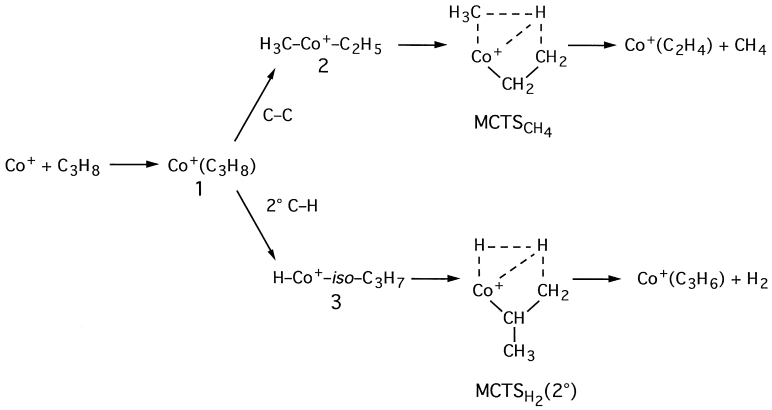

Scheme 1. Schematic reaction mechanism describing decay of long-lived $CoC_3H_8^+$ complexes. All CH_4 elimination arises from initial C–C bond insertion and all H_2 elimination arises from initial secondary C–H bond insertion by the metal ion.

and $Ni^+ + C_2H_6$ and C_3H_8 reactions.[7, 9–11] In the present study we only give the key stationary points whose properties are needed for statistical modeling under this mechanism. Those are the complex $Co(C_3H_8)^+$ and three multicentered transition states $MCTS_{CH_4}$, $MCTS_{H_2}(2°)$, and $MCTS_{H_2}(1°)$. Our computational approach follows that of an earlier study of $Co^+ + C_2H_6$.[10] Briefly, we use the B3LYP hybrid functional[46, 47] as implemented in Gaussian98.[48] This functional was combined with the standard D95** polarized, double-ζ basis set for carbon and hydrogen. For cobalt, the (14s9p5d) primitive set of Wachters[49] is supplemented with one diffuse p-function ($\alpha = 0.1219$) and one diffuse d-function according

0947-6539/00/0612-2236 $ 17.50+.50/0 Chem. Eur. J. 2000, 6, No. 12

to Hay,[50, 51] resulting in a (6211111|33121|411) → [8s5p3d] contraction. The transition states reported here were located by unconstrained geometry optimization using analytical gradients. The character (minimum or transition structure) of stationary points was determined by analytic evaluation of the force-constant matrix. Computed energies were corrected to ΔU at 0 K (equivalent to ΔH or ΔG at this temperature) by inclusion of zero-point vibrational energies.

As discussed in detail earlier,[10] the B3LYP ansatz gives the correct ordering for the Co^+ atomic states, with $3d^8$, ^3F below $3d^74s$, ^5F, but the excitation energy to the quintet excited state is overestimated by 5.2 kcal mol^{-1}. Energies of the $CoC_3H_8^+$ system are given relative to the asymptote $Co^+(3d^8,^3F)+C_3H_8$, using the atomic wavefunction resulting in integral orbital occupation pattern according to Hay.[52] In tests against experimental bond dissociation energies of Co^+ with ethane, ethylene, hydrogen, and alkyl groups, B3LYP tends to overestimate D_0 by 5–8 kcal mol^{-1}. The correction of Ricca and Bauschlicher[53] based on interpolation of the metal 3d populations does not improve the agreement and is not applied here.

The B3LYP results with this initial basis set are summarized in Table 4 under the heading "Model 1". Harmonic vibrational frequencies and rotational constants at the key stationary points (Table 5 and Table 6) will be used directly in the statistical rate calculations. B3LYP finds the $Co(C_3H_8)^+$ complex at −32.2 kcal mol^{-1}. This lies in good agreement with collision-induced dissociation experiments that find $D_0(Co^+–C_3H_8) = 30.9 \pm 1.4$ kcal mol^{-1}.[37] For comparison, a similar level of theory finds the $Ni(C_3H_8)^+$ complex at −35.6 kcal mol^{-1}.[7] The relative energies of the MCTSs along the lowest energy pathways to the three observed elimination products lie in qualitative accord with the experimental branching ratios. The lowest barrier is $MCTS_{H_2}(1°)$ at +1.1 kcal mol^{-1}, which involves secondary CH insertion followed by β-hydrogen migration leading to H_2 elimination, the predominant product. The second lowest barrier is $MCTS_{CH_4}$ at +1.9 kcal mol^{-1}, which involves C–C insertion followed by β-hydrogen migration leading to CH_4 elimination, the minority product. The location of $MCTS_{H_2}(2°)$ at +9.5 kcal mol^{-1} allows us to rule out this pathway to H_2 elimination at the low energies under study here. In addition, B3LYP has consistently found high barriers to *β-methyl* migration in Fe^+, Co^+, and Ni^+ reactions with alkanes,[7, 9–11, 45] so we rule out such pathways to CH_4 elimination.

Table 4. Energetics [kcal mol^{-1}] for models 1–3.[a]

Species	Model 1[b]	Model 2[c]	Model 3[d]
$CoC_3H_8^+$	−32.2	−38.8, −29.0[e]	−38.8, −29.0[e]
$MCTS_{CH_4}$	+1.9	−2.0	−2.0
$MCTS_{H_2}(2°)$	+1.1	−6.3	−4.7
$MCTS_{H_2}(1°)$[f]	+9.5	–	–

[a] Energies in kcal mol^{-1} relative to reactants, including ΔZPE_H corrections appropriate to $Co^+(d^8,^3F)+C_3H_8$. [b] From B3LYP density functional theory with the smaller basis set; see text for details. [c] Restriction on J imposed by the centrifugal barriers in exit channels. See text. [d] No restriction on J in exit channels. See text. [e] Two entries illustrate the range of energies for the collision complex that can produce complex decay time scales that match experiment, depending on the model used for internal rotational motions. See text. [f] This elimination path is not included in models 2 and 3.

Table 5. Harmonic vibrational frequencies [cm^{-1}] for Co^++C_3H_8 reaction from B3LYP theory with smaller basis set.

$CoC_3H_8^+$	$MCTS_{CH_4}$	$MCTS_{H_2}(2°)$	$MCTS_{H_2}(1°)$
3145	3207	3218	3207
3128	3166	3184	3166
3126	3144	3168	3144
3090	3103	3119	3103
2930	3074	3101	3074
2926	3064	2483	3064
2881	1872	1928	1872
2867	1709	1824	1709
1513	1517	1520	1517
1508	1488	1497	1488
1494	1470	1462	1470
1481	1450	1421	1450
1475	1417	1363	1417
1384	1350	1255	1350
1360	1202	1187	1202
1347	1145	1162	1145
1295	1062	1100	1062
1185	961	1042	961
1107	949	934	949
1049	901	926	901
893	740	839	740
875	622	620	622
871	541	544	541
752	480	449	480
506	383	418	383
445	374	372	374
352	290	360	290
203	191	277	191
203	122	226	122
130			

Table 6. Rotational constants [cm^{-1}] for Co^++C_3H_8 reaction from B3LYP theory with smaller basis set.

$CoC_3H_8^+$	$MCTS_{CH_4}$	$MCTS_{H_2}(2°)$	$MCTS_{H_2}(1°)$
0.281	0.375	0.252	0.337
0.112	0.113	0.159	0.096
0.084	0.094	0.110	0.084

The optimized geometries of the three MCTSs are shown in Figure 3. In the statistical modeling, the B3LYP energies for $MCTS_{H_2}(2°)$ and $MCTS_{CH_4}$ will be lowered substantially (models 2 and 3) to obtain quantitative agreement between statistical rate theory and experiment. This is just another manifestation of the fact that the asymptote involving transition metal atoms is most problematic to describe for the computational procedure applied, whereas relative energies of similarly bound species are computed with much better consistency.[10] However, the calculations are qualitatively correct in predicting that $MCTS_{H_2}(2°)$ lies below $MCTS_{CH_4}$ in Co^++C_3H_8, while the reverse occurred in Ni^++C_3H_8.[7] Accordingly, the ratio of H_2/CH_4 elimination reverses from about 3:1 for Co^+ to about 1:4 for Ni^+.

In order to allow for a direct comparison of structures and relative energies of the key transition structures for Fe^+, Co^+, and Ni^+ in the reaction with propane, we carried out additional B3LYP calculations with larger basis sets for $MCTS_{H_2}(2°)$ and $MCTS_{CH_4}$ for all three metals. The basis sets included 6-311++(2d,2p) on carbon and hydrogen plus

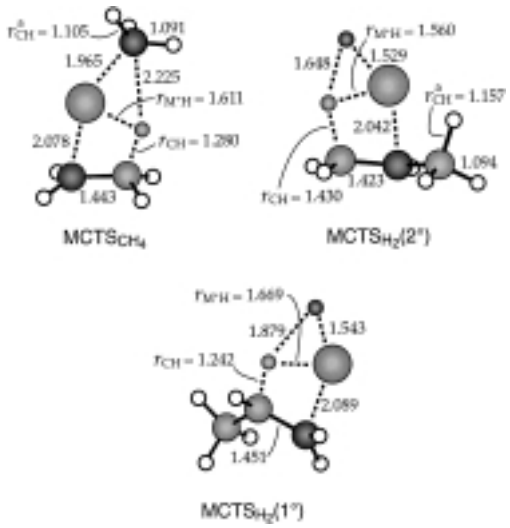

Figure 3. Geometries of multicenter transition states from B3LYP theory. See text.

6-311+G on cobalt (which is the Gaussian98 nomenclature for a modified Wachters-Hay all-electron basis contracted according to (6111111111 | 5111111 | 3111) → [10s7p4d] on the metal atoms).[49, 52, 54] Again the geometries were optimized and vibrational frequencies checked for a single imaginary value. The results are collected in Table 7. For the larger basis set, B3LYP theory finds MCTS$_{H_2}$(2°) *below* MCTS$_{CH_4}$ by 1.9 kcal mol^{-1} for Co^+ and MCTS$_{H_2}$(2°) *above* MCTS$_{CH_4}$ by 1.8 kcal mol^{-1} for Fe^+ and by 0.9 kcal mol^{-1} for Ni^+, in qualitative accord with the experimental branching ratios. For all three metals, the larger basis sets differentially stabilize MCTS$_{H_2}$(2°) relative to MCTS$_{CH_4}$(2°) by about 1 kcal mol^{-1} compared with the results using the smaller basis set. Interestingly, in the case of Fe^+ we found *two* transition structures following secondary CH insertion and β-hydrogen migration, which we call MCTS$_{H_2}$(2°) and MCTS$_{H_2}$(2°)′. Using the larger basis set, the former lies 1.6 kcal mol^{-1} lower in energy. These two transition structures differ primarily in the orientation of the β-methyl group. In MCTS$_{H_2}$(2°), the β-methyl group is involved in an agostic bond to Fe while in MCTS$_{H_2}$(2°)′ it is not. We searched for analogues of MCTS$_{H_2}$(2°)′ for Co^+ and Ni^+ starting from the optimized geometry for the Fe^+-based species but all attempts directly led back to the original MCTS$_{H_2}$(2°) geometries. Differences among the three metals will be discussed below.

Statistical Model for Decay of Co(C$_3$H$_8$)$^+$ Complexes

We apply the same statistical rate model that was successful for the Ni^++C_3H_8 and Ni^++*n*-C_4H_{10} reactions[5, 6] to the kinetics model of Scheme 1. The decay of Co(C$_3$H$_8$)$^+$ complexes **1** includes three parallel channels: dissociation back to reactants (k_{diss}); facile C–C bond insertion to intermediate **2**, leading to eventual CH_4 elimination (k_{CH_4}); and facile *secondary* CH bond insertion to intermediate **3**, leading to eventual H_2 elimination (k_{H_2}). Each elimination path involves sequential passage over first a bond insertion barrier and then a multicenter transition state (MCTS). The general solution of this kinetics model exhibits multiexponential decay. However, we assume that as in Fe^++C_3H_8 and Ni^++C_3H_8,[7, 11] each insertion well is shallow compared with complex **1** and the corresponding insertion transition state lies at least several kcal mol^{-1} below the MCTS. In this limit, we have shown that a simple steady-state approximation applies to each elimination channel and the overall decay of the complex becomes *exponential* with rate constant [Eq. (1)].

$$k_{tot}(E,J) = k_{diss}(E,J) + k_{CH_4}(E,J) + k_{H_2}(E,J) \quad (1)$$

In the steady-state limit, k_{CH_4} is given by Equation (2), where $W^{\dagger}$(MCTS$_{CH_4}$) is the sum of states at MCTS$_{CH_4}$ and ρ(**1**)

$$kCH_4 = \frac{W^{\dagger}(\mathrm{MCTS}_{CH_4})}{h\rho(\mathbf{1})} \quad (2)$$

is the density of states for the collision complex **1**. This expression is like an RRKM rate constant[55–57] for a single step in which the collision complex **1** reacts by crossing MCTS$_{CH_4}$ directly without intervening steps. The reason is that the shallow C–C insertion intermediate **2** has negligible effect on the rate under the steady-state approximation. An analogous expression holds for k_{H_2} in the steady-state limit. In this limit, the statistical model needs only the properties of the Co(C$_3$H$_8$)$^+$ complex, MCTS$_{CH_4}$, and MCTS$_{H_2}$(2°).

Table 7. Comparison of Fe^+, Co^+, and Ni^+ MCTSs.[a]

M$^+$	MCTS	Energy [kcal mol^{-1}]	Imag.Freq. [cm^{-1}]	Distances [Å][b] CH (methyl)	C=C (alkene)	M$^+$–H$_m$	–CH$_2$–H$_m$	CH$_3$–H$_m$, H–H$_m$
Fe^+	MCTS$_{CH_4}$	−6.2	396i	1.100	1.432	1.646	1.281	2.220
Fe^+	MCTS$_{H_2}$(2°)	−4.4	1039i	1.144	1.415	1.614	1.415	1.483
Fe^+	MCTS$_{H_2}$(2°)'	−2.8	929i	1.092	1.420	1.617	1.356	1.553
Co^+	MCTS$_{CH_4}$	+4.8	779i	1.098	1.430	1.611	1.274	2.272
Co^+	MCTS$_{H_2}$(2°)	+2.9	863i	1.157	1.413	1.562	1.418	1.672
Ni^+	MCTS$_{CH_4}$	+3.7	338i	1.096	1.416	1.507	1.354	2.317
Ni^+	MCTS$_{H_2}$(2°)	+4.5	755i	1.154	1.419	1.550	1.361	1.639

[a] B3LYP-optimized transition state energies and geometries using larger basis set (see text). Energies in kcal mol^{-1} relative to reactants including ΔZPE corrections. Calculated reactant asymptotes used are: Fe^+ (d^6s,^{6}D), Co^+(d^8,^{3}F), Ni^+(d^9,^{2}D). For Fe^+, the calculated d^6s,^{6}D state lies 5.0 kcal mol^{-1} above d^7,^{4}F whereas experiment finds d^7,^{4}F below d^6s,^{6}D by 5.6 kcal mol^{-1}. [b] CH methyl refers to the longest CH bond within the methyl rotor placed α relative to MCTS$_{CH_4}$ or β relative to MCTS$_{H_2}$(2°) or MCTS$_{H_2}$(2°)'; C=C refers to the incipient alkene CC bond; H$_m$ refers to the hydrogen migrating to meet methyl in MCTS$_{CH_4}$ or the other hydrogen in MCTS$_{H_2}$(2°) or MCTS$_{H_2}$(2°)'.

0947-6539/00/0612-2238 $ 17.50+.50/0 *Chem. Eur. J.* **2000**, *6*, No. 12

The details of the RRKM calculations were previously described.[7] Each RRKM rate constant is given by Equation (3), where n is the reaction path degeneracy, $W^\dagger$ is the

$$k(E,J) = n\frac{W^\dagger(E - E_0 - E_r^\dagger(J))}{h\rho(E - E_r^\dagger(J))} \quad (3)$$

sum of vibration–rotation states at the transition state, and ρ is the density of vibration–rotation states for the reactant. The Beyer–Swinehart direct count algorithm[58, 59] is used to evaluate the density and sum of states. We define E as the total reactant energy including collision energy, any electronic energy of Co^+, and any internal energy of C_3H_8. E_0 is the activation energy. $E_r(J)$ and $E_r^\dagger(J)$ are inactive rotational energies of reactant and transition state unavailable for passage over the barrier. The amount of energy tied up in overall rotation of the complex changes as the reaction proceeds because the moments of inertia change. We approximate the total angular momentum J of the complex as equal to the orbital angular momentum l brought to the complex by the ion–molecule collision, which is appropriate for internally cold reactants. Lacking information about excited state surfaces, we assume the reaction occurs entirely on the adiabatic ground electronic state.

The treatment of methyl torsions in the initial collision complex and MCTSs directly affects state-counting and the reaction path degeneracy. We prefer the same treatment that was most successful for the Ni^++C_3H_8 reaction.[7] All methyl torsions are treated as free rotation except for the two methyl torsions at the orbiting transition state in the entrance channel, for which the total energy is not much larger than the torsional energy barriers of about 3 kcal mol^{-1}. The resulting reaction path degeneracies are 9 for $k_{diss'}$ 6 for $k_{CH_4'}$ and 6 for k_{H_2}. Tables 5 and 6 list B3LYP vibrational frequencies and rotational constants for the initial collision complex and MCTSs used in RRKM calculations. Alternatively, we can treat the methyl rotors of the complex as threefold degenerate harmonic vibrations, which substantially alters ρ(**1**). In this latter treatment, we are forced to raise the energy of the complex **1** in order to match the experimental lifetime, as described below.

In an attempt to understand the possible effects of a high exit-channel centrifugal barrier on the detailed dynamics of H_2 elimination, we employ two different models. As suggested by van Koppen and co-workers,[16, 41] the low mass and small polarizability of H_2 could make centrifugal effects particularly important in the exit channel of H_2 elimination path. In model 2, we assume that $J = l = l'$, where J is the total angular momentum of the complex, l is the initial orbital angular momentum of collision, and l' is the orbital angular momentum in the exit channel for H_2 elimination. That is, we have assumed no rotational excitation of the molecular products $Co(C_3H_6)^+$+H_2. Thus complexes with J larger than l'_{max} dissociate to H_2 in model 2, where l'_{max} is the largest l' that can cross the centrifugal barrier in the exit channel. For the CH_4 elimination channel, the analogous exit-channel effects are present only at higher collision energy due to the heavier reduced mass and larger polarizability.

However, simple kinematics suggests that much of the angular momentum present as overall rotation of the complex likely remains as rotation of the $Co(C_3H_6)^+$ fragment, since the center of mass of the complex and that of the $Co(C_3H_6)^+$ fragment nearly coincide. Thus in model 3 we write $\vec{J} = \vec{l} = \vec{l'} + \vec{j'}$. In this vector equation, non-zero j' (rotation of fragment) can allow high-J complexes to dissociate to H_2 over relatively low centrifugal barriers (low l'), with j' absorbing much of the total angular momentum,[57] as occurs in phase space theory. Our model 3 assumes *no* centrifugal effects in the exit channel for H_2 elimination ($l' = 0$). All complexes with $J < J_{max}$ can form H_2, where J_{max} is the largest angular momentum that can cross the relevant MCTS. Thus models 2 and 3 are extreme cases; phase space theory would lie somewhere in between. The same assumption is applied to the CH_4 elimination channel in model 3.

Adjustment of model parameters

Model 1 uses the B3LYP energetics without adjustment (Table 4). These energies cannot fit experiment at all. The absolute elimination cross section is negligible compared with experiment even at 0.21 eV and the CH_4/H_2 branching ratio comes out 1.1, in contrast to the experimental value of 0.36. To fit the absolute reaction efficiency of 6% at 0.21 eV, it is necessary to lower $MCTS_{H_2}(2^\circ)$ to a value of near -6.3 kcal mol^{-1}, which is 7.4 kcal mol^{-1} below the result obtained with B3LYP ($+1.1$ kcal mol^{-1}). To fit the 1:3 branching ratio of CH_4:H_2 elimination, we must then lower $MCTS_{CH_4}$ to -2.0 kcal mol^{-1}, which is 3.9 kcal mol^{-1} below the B3LYP result of $+1.9$ kcal mol^{-1}. These adjustments, which we call model 2, assume $j' = 0$ so that l'_{max} sets the cutoff on the total angular momentum that can produce H_2. In model 3, we assume that all J that cross $MCTS_{H_2}(2^\circ)$ produce H_2 ($l' = 0$, no exit-channel effects). This allows us to raise the energy of $MCTS_{H_2}(2^\circ)$ to -4.7 kcal mol^{-1}.

Experiment shows that for $E_t = 0.21$ eV, a majority of the initial collision complexes revert to Co^++C_3H_8 reactants and substantial decay occurs on a 500 ns–20 μs time scale. The dual entry for the energy of the complex **1** under models 2 and 3 in Table 4, -38.8 and -29.0 kcal mol^{-1}, shows two very different values which can bring k_{diss} into good agreement with experiment. If the two soft bends are treated as harmonic vibrations with 130 and 203 cm^{-1} frequencies from Table 5, then the binding energy of the complex must be increased to -38.8 kcal mol^{-1} to achieve large enough ρ(**1**). Alternatively, if the bending motions of complex **1** are treated as two-dimensional free internal rotation of C_3H_8 relative to Co^+, then the binding energy must be decreased to -29.0 kcal mol^{-1}. These two energies roughly bracket the physically reasonable limits, quite independent of other energetic adjustments of the model. Evidently, we cannot determine the binding energy of complex **1** very accurately from our lifetime data. Of the two idealized models, we prefer the free rotor since the internal energy of the complex far exceeds the methyl rotor barriers of 3 kcal mol^{-1} or less. The corresponding value of -29.0 kcal mol^{-1} is close to the estimate of 30.9 kcal mol^{-1} for Co^+–C_3H_8 binding energy

from a threshold collisional activation study.[37] However, interpretation of those experiments is presumably subject to much the same modeling uncertainty that we confront here.

Predictions of models 2 and 3

With the energetics of models 2 and 3 constrained using the experimental reaction efficiency, complex lifetime, and H_2/CH_4 branching ratios for $Co^+ + C_3H_8$ at 0.21 eV, we can compare the detailed predictions of both models with other experimental data. In Figure 4 we display the J dependence of

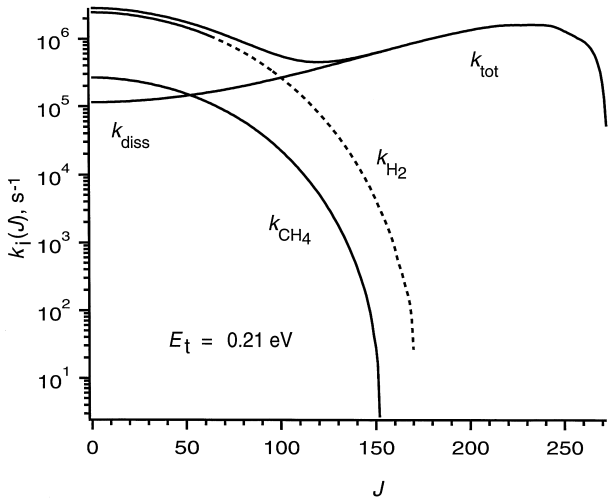

Figure 4. Dependence of three parallel decay rates and total decay rate on J for model 2 parameters at $E_t = 0.21$ eV. Dashed line assumes no centrifugal effects in the H_2 exit channel, as in Model 3. See Table 4 and text.

the three parallel decay rates k_{diss}, k_{CH_4},and k_{H_2} for model 2 at 0.21 eV. The Langevin cutoff on the maximum $J = l$ lies at 272 for this energy. The three parallel rates are summed to form the overall complex decay rate $k_{tot}(E,J)$ For $k_{H_2'}$ the dotted portion of the curve represents the collision complexes that cannot eliminate H_2 due to angular momentum constraints in the exit channel; in model 3 such complexes contribute to the H_2 branching fraction. As for $Ni^+ + C_3H_8$, elimination of CH_4 and H_2 occurs primarily from complexes formed at low J values (low impact parameters). While k_{CH_4} and H_2 vary over many decades with J and k_{diss} varies over two decades, their sum k_{tot} varies less than one order of magnitude, from 10^5 to $10^6\,s^{-1}$. The two parallel decay rates k_{CH_4} and k_{H_2} decrease as J increases. The cutoffs at high J arise from the differential effects of the centrifugal potentials; this is purely an effect of the mass distribution on the sum of states. The centrifugal barrier at $MCTS_{CH_4}$ cuts off k_{CH_4} at $J_{max} = 150$, which sets the limit on the largest J that can contribute to the $CoC_2H_4^+ + CH_4$ products. For the H_2 elimination channel, the centrifugal barrier at $MCTS_{H_2}(2^\circ)$ cuts off k_{H_2} at $J_{max} = 170$. However, due to the small reduced mass of the $CoC_3H_6^+ + H_2$ product and the low polarizability of H_2, the high-J cutoff for overall H_2 elimination might now occur not at $MCTS_{H_2}(2^\circ)$, but at the exit channel. In the extreme limit $l' = J$ (model 2) with the estimate of 15.0 kcal mol^{-1} for the exothermicity,[37] the centrifugal barrier in the exit channel sets a more stringent cutoff at $J \leq 65$ on k_{H_2}, as shown in Figure 4. The CH_4 elimination channel begins to suffer the same type exit-channel effects only near $E_t = 1$ eV. The J dependence of k_{diss} is opposite that of the elimination rates, that is, k_{diss} increases with increasing J. As $CoC_3H_8^+$ dissociates to $Co^+ + C_3H_8$, mass moves away from the center of mass, decreasing the centrifugal barrier at the orbiting transition state compared with the complex **1**.

Within the steady-state, parallel decay approximations, the time-resolved, J-averaged formation rate for each decay channel is given by Equation (4), where i stands for one of

$$\frac{1}{[CoC_3H_8^+]_0}\left\langle\frac{dn_i}{dt}\right\rangle = \sum_{J=0}^{J_{max}} P(J)k_i(E,J)e^{-k_{tot}(E,J)t} \qquad (4)$$

three channels (dissociation, CH_4 elimination, or H_2 elimination); n_i is the number density of the product i; $[CoC_3H_8^+]_0$ is the number density of the complexes at $t = 0$; l_{max} is the largest orbital angular momentum that can penetrate the orbiting transition state determined by the Langevin cross section; and $P(J) = 2J/l_{max}^2$. Direct comparison with the time-resolved experiments is made by integrating these equations over various time intervals, as described in detail elsewhere.[7]

In Tables 8 and 9, we compare the predictions of the adjusted models 2 and 3 with experimental time-dependent branching fractions integrated over the two experimental time windows, 2 – 10 μs and 6 – 24 μs. We have properly averaged over the distribution of collision initiation times. The energetics of models 2 and 3 were adjusted to give good agreement for the 2 – 10 μs window at 0.21 eV (Table 8). The agreement for the 6 – 24 μs time window at 0.21 eV is substantially better for model 3 (no exit channel centrifugal effects) than for

Table 8. Branching ratios versus experiment, $t = 2 - 10$ μs after collision.[a]

	E_t [eV]	$CoC_2H_4^+ + CH_4$	$CoC_3H_6^+ + H_2$	$CoC_3H_8^+$
experimental[a]	0.21	15 ± 4	42 ± 5	43 ± 9
model **2**[b]	0.21	14	40	46
model **3**[b]	0.21	15	42	43
experimental[a]	0.01	2.0 ± 0.5	16 ± 2	82 ± 2
model **2**[b]	0.01	1	33	66
model **3**[b]	0.01	< 1	8	92

[a] Experimental averages over this time interval in the kinetics model. [b] See Table 4 and text.

Table 9. $CoC_3H_8^+$ fragmentation pattern versus experiment, $t = 6 - 24$ μs after collision.[a]

	E_t (eV)	$Co^+ + C_3H_8$	$CoC_2H_4^+ + CH_4$	$CoC_3H_6^+ + H_2$
experimental[a]	0.21	72 ± 15	< 2[c]	27 ± 3
model **2**[b]	0.21	93	7	< 1
model **3**[b]	0.21	86	4	10
experimental[a]	0.01	64 ± 9	< 2[c]	34 ± 3
model **2**[b]	0.01	5	2	93
model **3**[b]	0.01	6	4	90
model **3′**[d]	0.01	67	3	30

[a] Experimental averages over this time interval in the kinetics model. [b] See Table 4 and text. [c] Upper bound only. [d] Same as model 3, but includes 1 kcal mol^{-1} additional internal energy to mimic vibration/rotation energy in propane reactant.

0947-6539/00/0612-2240 $ 17.50+.50/0 *Chem. Eur. J.* **2000**, *6*, No. 12

model 2. The latter model produces essentially no delayed H_2, while experiment finds 27%. Model 3 predicts 10%.

In Figure 5, we show plots of the three parallel decay rates and k_{tot} versus J for the lower collision energy, nominal 0.01 eV. Now k_{H_2} is much larger than k_{diss} or k_{CH_4} for all J. The total decay rates plummet into the range $10^3-10^5\,s^{-1}$, which

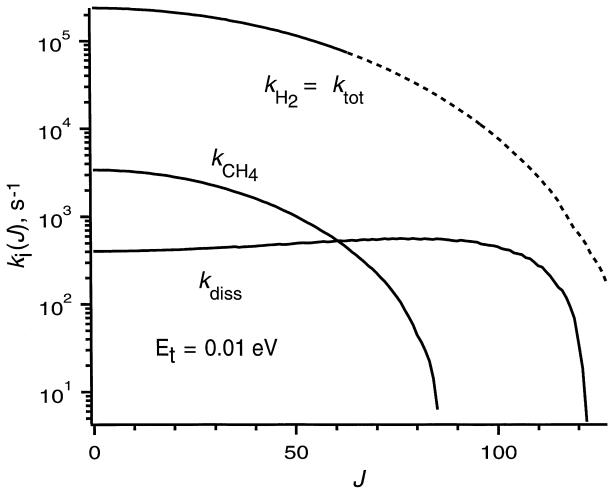

Figure 5. Dependence of three parallel decay rates and total decay rate on J for model 2 parameters at $E_t = 0.01$ eV. Dashed line assumes no centrifugal effects in the H_2 exit channel, as in model 3. See Table 4 and text.

would be too slow for us to observe extensive complex decay on the time scale of our experiment. This is qualitatively consistent with the data of Figure 1, which shows predominantly $CoC_3H_8^+$ adducts in the 2–10 μs time window at nominal 0.01 eV and a much larger ratio of H_2/CH_4 at this low collision energy than at 0.21 eV. The quantitative comparison is again somewhat better for model 3 (no exit channel effect) than model 2. The experimental fraction of adducts in the 2–10 μs time window increases from 43% at 0.21 eV to 82% at 0.01 eV. Models 2 and 3 predict 66% and 92%, respectively, at 0.01 eV (Table 8). In the longer time window 16–24 μs for 0.01 eV (Table 9), *neither* model captures the observed dominance of dissociation back to $Co^+ + C_3H_8$, while both models obtain sensibly large ratios of H_2/CH_4 elimination. A similar problem arose in modeling the nominal 0.01 eV data for $Ni^+ + C_3H_8$, probably because k_{diss} is extremely sensitive to internal energy in the complex. If we add 1 kcal mol^{-1} of internal energy to mimic vibration/rotation energy in the propane reactant (model 3′ in Table 9), the calculated ratio of Co^+:$CoC_2H_4^+$:$CoC_3H_6^+$ changes dramatically from 6:4:90 to 67:3:30, in sensible agreement with experiment. Addition of 1 kcal mol^{-1} = 0.04 eV of collision energy, mimicking imperfections in the experimental velocity selection, has a similar effect.

In Figure 6, we compare the prediction of models 2 and 3 as a function of collision energy with the absolute experimental elimination cross-section data (sum of CH_4 and H_2) from Armentrout and co-workers.[37] The reaction efficiency at 0.05 eV predicted by models 2 and 3 is 12% and 18%, respectively, in rough agreement with the experimental reaction efficiency of 8 ± 5%. Discussions with Professor

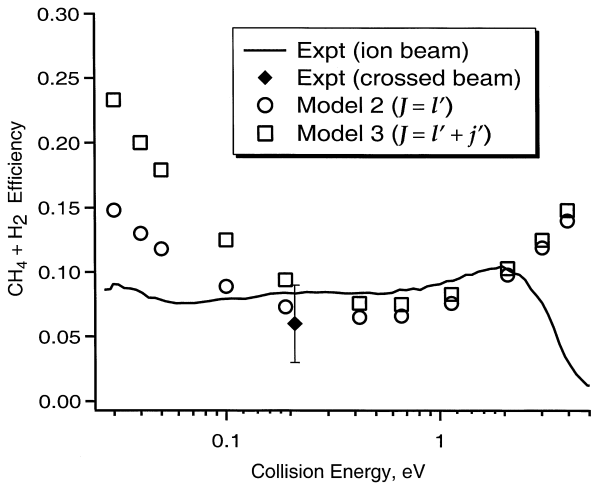

Figure 6. Comparison of total H_2 and CH_4 elimination efficiency vs E_t between models 2 and 3 and experiment. Solid line is data of Armentrout and co-workers;[37] diamond is single result from present work.

Armentrout indicate that the reliability of the cross-section data diminishes rapidly below 0.05 eV, so the increase in reaction efficiency of the models towards lower energy may be a real effect. The experimental curve shows a hint of the positive curvature predicted by both models towards higher energy. For $Ni^+ + C_3H_8$, both the experimental curve and the predictions of the best model showed the same strong positive curvature in the region 0.02–1 eV.[7] Beyond 2 eV the experimental data fall off abruptly, but the model results do not, probably due to the onset of an endothermic fragmentation channel missing from the model. The two models differ substantially at low energy, where H_2 dominates over CH_4, but converge towards higher collision energy where CH_4 elimination becomes much more important. More accurate cross section data at very low E_t would help distinguish among models of H_2 exit-channel effects.

Both models 2 and 3 capture the change in elimination product branching with collision energy quite well (Figure 7).

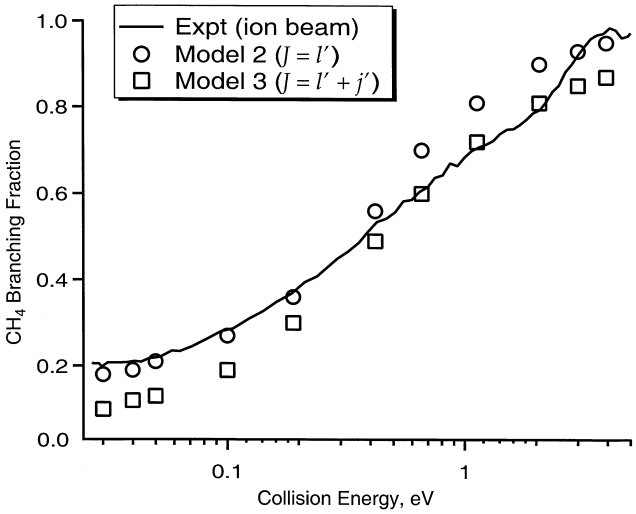

Figure 7. Comparison of CH_4 elimination branching fraction versus E_t between models 2 and 3 and experiments of Armentrout and co-workers (solid line, reference [37]).

In experiment and in both models, the absolute cross section for dehydrogenation decreases rapidly with collision energy, while the demethanation cross section decreases more slowly at first and then reaches a plateau near 0.1 eV. The experimental observations were interpreted as arising from two pathways to CH_4 elimination with barriers located at -0.08 ± 0.08 eV and $+0.05 \pm 0.04$ eV relative to reactants.[37] However, our models 2 and 3 both lack such a second pathway to CH_4 elimination but find the CH_4 branching fraction increasing with collision energy in good agreement with experiment. The reason again lies in the conservation of angular momentum. $MCTS_{CH_4}$ and $MCTS_{H_2}(2^\circ)$ differ substantially in their moments of inertia (Table 6). $MCTS_{H_2}(2^\circ)$ has the larger rotational constants and thus larger centrifugal barrier for a given *J*. Consequently, at higher energy a larger range of *J* can cross $MCTS_{CH_4}$ than $MCTS_{H_2}(2^\circ)$, causing the growing preference for CH_4 elimination over H_2 elimination at higher energies. In qualitative agreement with the B3LYP results, it appears that there is no need to invoke a second CH_4 elimination pathway, at least below 1 eV collision energy.

Discussion

Models 2 and 3 achieve good semiquantitative agreement between statistical rate theory and a wide variety of experimental data by placing $MCTS_{CH_4}$ at -2.0 kcal mol^{-1} and $MCTS_{H_2}(2^\circ)$ at -6.3 kcal mol^{-1} (model 2) or $MCTS_{CH_4}$ at -2.0 kcal mol^{-1} and $MCTS_{H_2}(2^\circ)$ at -4.7 kcal mol^{-1} (model 3). Within the context of the model and its assumptions, we estimate that the data constrain the energies of these MCTSs to ± 2 kcal mol^{-1}. It is difficult to assess the possible effects of anharmonicity and electronic degeneracy. The downward adjustment of the B3LYP calculated energies by 3.9 kcal mol^{-1} for $MCTS_{CH_4}$ and by 5.8–7.4 kcal mol^{-1} for $MCTS_{H_2}(2^\circ)$ is quite similar to the adjustments needed in $Ni^+ + C_3H_8$ ($MCTS_{CH_4}$ downward by 5.6 kcal mol^{-1} and $MCTS_{H_2}(2^\circ)$ downward by 7.2 kcal mol^{-1}).[7] As described in detail elsewhere,[9, 10] for Fe^+ and Co^+, B3LYP systematically *overestimates* binding energies of stable species such as M^+–CH_3, M^+–C_2H_5, and $M^+(C_2H_4)$ by 3–7 kcal mol^{-1}. Yet B3LYP seemingly *underestimates* the net binding in key MCTSs by 4–7 kcal mol^{-1}.

This effect is due in part to errors in describing the relative Co^+ atomic $d \rightarrow s$ excitation energies. As already noted, for the smaller basis set used here B3LYP overestimates the promotion energy from the $3d^8$,^{3}F ground state to the $3d^7 4s$,^{5}F excited state by 5.2 kcal mol^{-1}. With the larger basis set, the error in the same atomic promotion energy increases to 7.4 kcal mol^{-1}. The energy difference between $MCTS_{CH_4}$ and $MCTS_{H_2}(2^\circ)$ stays nearly constant but the energy of both MCTSs increases by 2–3 kcal mol^{-1} relative to the value for $Co^+ + C_3H_8$ (i.e., the larger basis set results demand an even larger downward adjustment to achieve agreement with experiment). Part of this error can probably be related to the deviations observed for the atomic state splittings, since the binding in the MCTSs involve partial occupation the 4s orbital due to s/d-hybridization. One could tentatively argue then, that the well documented preference of B3LYP to favor d^n over $d^{n-1}s^1$ atomic states leads to too high barriers for the transition structures, where atomic s/d-hybridization is involved.[4] This, however, cannot be the complete story, because in Ni^+, the analogous error in atomic promotion energy is only 4.9 kcal mol^{-1} (larger basis set) but it is still necessary to adjust the MCTS energies downward by 6–7 kcal mol^{-1}.[7] As already alluded to above, errors in the theoretical description of the atomic asymptote are quite large, and this is the most problematic region in the potential energy surface for the theoretical assessment.

Our adjusted model energetics lie in good agreement with barrier heights inferred from recent threshold collision-induced dissociation experiments by Armentrout and co-workers.[37] They examined the forward reaction $Co^+ + C_3H_8$, the threshold collisional activation of cold $CoC_3H_8^+$ complexes, and the reverse of the dehydrogenation and demethanation reactions. From all of this work they infer a rate-limiting barrier for dehydrogenation at -6.7 ± 2.3 kcal mol^{-1} relative to the $Co^+ + C_3H_8$ asymptote. This stands in very good agreement with our best adjusted energy of -6.3 kcal mol^{-1} for $MCTS_{H_2}(2^\circ)$ in model 2 and reasonable agreement with the value -4.7 kcal mol^{-1} in model 3. For demethanation, they inferred two barriers at -1.8 ± 1.8 kcal mol^{-1} and $+1.2 \pm 0.9$ kcal mol^{-1} relative to $Co^+ + C_3H_8$. The location of the lower barrier agrees very well with the adjusted energy of -2.0 kcal mol^{-1} for $MCTS_{CH_4}$ (for either model 2 or 3). As described above, with the help of the statistical model plus angular momentum conservation we found no need to invoke a second CH_4 elimination pathway to explain the CH_4/H_2 branching versus E_t.

In addition, van Koppen, et. al[41] earlier measured kinetic energy release distributions (KERDs) in both H_2 and CH_4 channels from metastable decay of long-lived $CoC_3H_8^+$ complexes formed at thermal energy. From analogous statistical modeling based on the idea that CH bond insertion is rate-limiting and produces both H_2 and CH_4 products, they placed the rate-limiting barrier at -2.3 ± 0.7 kcal mol^{-1}. Perhaps coincidentally,[11] this is quite similar to our best adjusted energy of $MCTS_{CH_4}$, which produces only CH_4 in our models.

An important assumption in our work is that the key MCTSs lie well *above* the initial bond insertion TSs. As discussed before,[7] our experiments combined with statistical modeling cannot distinguish these two possibilities. However, we strongly prefer placing each MCTS above the corresponding initial insertion TS for three reasons. First, B3LYP theory clearly predicts that the MCTS is the highest potential energy point along each elimination pathway for closely related reactions: the same energy order was found in B3LYP calculations on Fe^+ and $Ni^+ + C_3H_8$.[7, 11] Second, a recent CASSCF study of the same $Co^+ + C_3H_8$ reaction found the relevant MCTSs 3–10 kcal mol^{-1} above the corresponding bond insertion TSs.[60] Third, the isotopic labeling experiments for the $Co^+ + C_3H_8$ reaction by Armentrout and co-workers[37] support this conclusion. They studied the two labeled reverse reactions $Co^+(C_3H_6) + D_2$ and $CoC_2H_4^+ + CD_4$ to make Co^++labeled propane in the ion beam apparatus. The reverse reactions to produce Co^+ are inefficient but observable. Importantly, what is not observed is isotopically scrambled

  0947-6539/00/0612-2242 $ 17.50+.50/0 *Chem. Eur. J.* **2000**, *6*, No. 12

reactants, for example, $Co^+(C_3H_5D)$+HD or $CoC_2H_3D^+$ + CD_3H. If, for example, the initial CH insertion TS lay above then in the $Co^+(C_3H_6)$+D_2 reaction we would expect the long-lived $Co^+(C_3H_6)(D_2)$ to cross and re-cross $MCTS_{H_2}(2^\circ)$ many times before finally managing to cross initial CH insertion TS to produce $Co^+(C_3H_6D_2)$ and then Co^++$C_3H_6D_2$ very inefficiently. Multiple crossings of $MCTS_{H_2}(2^\circ)$ would produce significant $Co^+(C_3H_5D)$+HD scrambling product, which is not observed. The negative observation is easily explained if $MCTS_{H_2}(2^\circ)$ lies above the initial CH insertion TS. Similar arguments hold for the CH_4 channel.

How generally significant are MCTSs of the kind that evidently control the reactivity of Fe^+, Co^+, and Ni^+ with alkanes? It is possible that they are important only for the late 3d series cations. The MCTSs seemingly provide alternatives to stepwise rearrangement mechanisms that pass through stable intermediates of the form $M^+(R)(R')$(alkene), where R and R′ are hydrogen or an alkyl group. In the 3d series, the creation of two σ bonds to R and R′ involve s/d hybridization on the metal atom. With seven, eight, and nine valence electrons (for Fe^+, Co^+, and Ni^+) and with the 4p orbitals too high in energy to contribute, the metal atom has respectively three, two, and one additional singly occupied 3d orbitals which could accept charge density to accomplish binding to the alkene. Evidently a "half-bond" to alkene is not strong enough to produce a stable intermediate of the form $M^+(R)(R')$(alkene). Pairing two electrons in Fe^+ or Co^+ could provide an empty acceptor orbital, but the loss of exchange energy is too expensive in the late 3d series. The alternative is the concerted pathway over an MCTS to the exit-channel complex. Armentrout[61] has speculated that in the 4d series (e.g., Ru^+ and Rh^+) spin-pairing and the traditional stepwise mechanism may provide the lowest energy pathways due to smaller promotion energies to low-spin atomic states than in the 3d series. Again on the left-hand side of the transition metal block where empty d orbitals are plentiful, the MCTS mechanism may not compete with the stepwise mechanism. Further electronic structure calculations are needed to test these qualitative ideas.

It remains unclear why Fe^+ and Ni^+ strongly favor CH_4 elimination over H_2 elimination (by 4:1 in both cases) while Co^+ favors H_2 over CH_4 (by 3:1). The B3LYP calculations capture the correct trend in MCTS relative energies with both the smaller (Table 4) and larger (Table 7) basis sets. At our highest level of theory (Table 7), the energy difference between $MCTS_{H_2}(2^\circ)$ and $MCTS_{CH_4}$ is $+1.8$ kcal mol^{-1} in Fe^+, -1.9 kcal mol^{-1} in Co^+, and $+0.9$ kcal mol^{-1} in Ni^+, in qualitative accord with the experimental branching preferences. In a recent theoretical investigation on Co^++C_3H_8 by Fedorov and Gordon[60] the MCTS geometries have been optimized at the complete active space self-consistent field (CASSCF) level of theory, whereas final energies have been obtained using multi-reference second-order perturbation theory (MRMP2). The picture emerging for the reaction pathways is qualitatively in accord with our findings, with $MCTS_{H_2}(2^\circ)$ and $MCTS_{CH_4}$ controlling product branching. The geometries of the key MCTSs in both studies look qualitatively similar. In contrast to B3LYP, the MRMP2 results found $MCTS_{H_2}(2^\circ)$ *above* $MCTS_{CH_4}$ by 1.7 kcal mol^{-1}. The basis set used in these calculations is, however, rather small for *post*-HF theory and this relative energy is probably subject to changes if larger basis sets, improved active spaces, or other than CASSCF geometries are used. Overall we have been quite pleased by the ability of density functional theory to provide very reasonable *relative* energies of key transition states, fully in accord with the trends observed experimentally.

A detailed examination of our MCTS geometries for the different metals does not provide easy clues to the underlying causes of the subtle energy differences that control product branching. A β-methyl agostic interaction[62, 63] is evident in $MCTS_{H_2}(2^\circ)$ for all three metals. As judged by the β-methyl CH bond lengths (Table 7), the strength of this interaction varies only slightly from Fe^+ to Co^+ to Ni^+. While this interaction presumably lowers the energy of $MCTS_{H_2}(2^\circ)$ relative to $MCTS_{H_2}(1^\circ)$ for all three metals, it does not seem to explain the special stability of $MCTS_{H_2}(2^\circ)$ relative to $MCTS_{CH_4}$ in Co^+. For all three metals the α-methyl agostic interaction imaginable in $MCTS_{CH_4}$ is evidently very weak, if present at all, judging from the CH bond lengths (cf. Table 7).

Based on the valence electron counts described above, we might expect Fe^+ and Co^+ to be better suited to make *multiple partial bonds* by virtue of their larger number of half-filled d orbitals. Yet there is no clear evidence of this in the MCTS geometries optimized with the larger basis set. Instead, the Fe^+, Co^+, and Ni^+ variants of both $MCTS_{H_2}(2^\circ)$ and $MCTS_{CH_4}$ are remarkably similar in the key bond lengths (Table 7). In all cases, the M^+–H_m distance (where H_m is the migrating hydrogen atom) is very short, comparable to a full σ bond length. Both $MCTS_{H_2}(2^\circ)$ and $MCTS_{CH_4}$ are "early" transition states (reactant-like) in the sense that the CH_2–H_m bond being broken is nearer a normal σ bond length than the CH_3–H_m or H–H_m bond being formed. Based on bond lengths, to a first approximation the metal atom makes three single bonds (to H_m, to H or CH_3, and to the alkyl group) in all cases. The geometry of these three bonds about the metal is most often nearly planar. The two exceptions are the $MCTS_{CH_4}$ geometries for Co^+ and Ni^+, which are somewhat pyramidal about the metal (dihedral angle C-M-H_m-C equal to 42° and 62°, respectively).

For Fe^+, but not for Co^+ or Ni^+, we found a second variant of the transition structure leading to H_2 elimination, which we called $MCTS_{H_2}(2^\circ)'$. Using the larger basis set, it lies 1.6 kcal mol^{-1} higher than $MCTS_{H_2}(2^\circ)$ and differs geometrically only by a rotation of the β-methyl group, such that no agostic interaction is present. The energy difference can be taken as a rough indication of the stabilization due to this interaction. In RRKM modeling of reaction rates, two transition state isomers separated by a small energy barrier compared with the internal energy of the molecule should be treated as a single transition state.

Conclusion

The combination of electronic structure theory, statistical rate theory, and a variety of experimental measurements provides a remarkably detailed view of the Co^++C_3H_8 reaction. Our model based on B3LYP calculations can explain the range of

experimental time scales, the product branching fractions, and total cross section vs kinetic energy. The basic mechanisms by which Fe^+, Co^+, and Ni^+ react with all linear hydrocarbons now seem quite similar, involving low barriers to C–C or C–H bond insertion and rate-limiting multicenter transition states. However, quite subtle differences in electronic structure among the three metal cations alter the relative energetics of the key multicenter transition states, leading to dramatic shifts in branching between H_2 and CH_4 elimination. An important new goal for theory would be to attempt to analyze the energetic contributions of agostic interactions, partial binding to the migrating hydrogen atom, and exchange stabilization to overall MCTS stability.

Once again in $Co^+ + C_3H_8$, statistical rate theory on a single potential energy surface (adiabatic reaction dynamics) seems to provide an adequate description of the reaction dynamics. The largest remaining issue is the role of angular momentum conservation in the H_2 exit channel. Both model 2 (strong centrifugal barrier effects cutting off H_2 for high J) and model 3 (no such effects) fit the data reasonably well, although model 3 is slightly preferred. Highly accurate H_2 elimination cross section measurements below 0.1 eV collision energy might help resolve this issue, but kinetic energy release distributions (KERDs) for the $CoC_3H_6^+ + H_2$ products probe it more directly.

Bowers and co-workers[41] measured the KERD for both the CH_4 and H_2 channels from metastable decay of long-lived $CoC_3H_8^+$ complexes. The KERD for CH_4 elimination peaked near zero energy but was *colder* than the predictions of unrestricted phase space theory, consistent with orbital angular momentum constraints at $MCTS_{CH_4}$. The KERD for H_2 elimination was bimodal with a much *larger* mean kinetic energy than statistical theory predicts. The H_2 KERD thus seems to contradict the same adiabatic statistical rate models that can explain so much other data. It is possible that the measurements included contributions from complexes formed by excited-state Co^+ reactants, since an electron impact source was used. That might explain the hot, bimodal KERD for H_2 elimination products.

To test this possibility, we are presently modifying our crossed-beam experiment to include velocity map imaging of the ionic products. This will provide KERDs of mass-selected products formed from electronic-state specific reactants for $Co^+ + C_3H_8$ and a variety of other interesting ion–molecule reactions.

Acknowledgement

J.C.W. thanks the National Science Foundation (CHE-9616724) and the Donors of the Petroleum Research Foundation (PRF-33441-AC6) for support of this research. S.S.Y. acknowledges support from a Lubrizol Fellowship. M.C.H. gratefully acknowledges a Feodor Lynen fellowship from the Alexander von Humboldt Stiftung and a Liebig fellowship from the Fonds der Chemischen Industrie. W.K. acknowledges support by the Gesellschaft von Freunden der Technischen Universität Berlin and the Fonds der Chemischen Industrie. We also thank Prof. Peter Armentrout for providing details of his published data and for helpful discussions.

[1] K. Eller, H. Schwarz, *Chem. Rev.* **1991**, *91*, 1121.
[2] P. B. Armentrout, T. Baer, *J. Phys. Chem.* **1996**, *100*, 12866–12877.
[3] J. C. Weisshaar in *State-Selected and State-to-State Ion-Molecule Reaction Dynamics* (Ed.: C. Y. Ng), Wiley, New York, **1992**.
[4] W. Koch, M. C. Holthausen, *A Chemist's Guide to Density Functional Theory,* Wiley-VCH, Weinheim, Germany, **2000**.
[5] M. R. A. Blomberg, P. E. M. Siegbahn, S. S. Yi, R. J. Noll, J. C. Weisshaar, *J. Phys. Chem. A* **1999**, *103*, 7254–7267.
[6] R. J. Noll, S. S. Yi, J. C. Weisshaar, *J. Phys. Chem. A.* **1998**, *102*, 386.
[7] S. S. Yi, M. R. A. Blomberg, P. E. M. Siegbahn, J. C. Weisshaar, *J. Phys. Chem. A.* **1998**, *102*, 395.
[8] E. L. Reichert, S. S. Yi, J. C. Weisshaar, *Int. J. Mass Spec. Ion Phys.* **2000**, *195/196*, 55–69.
[9] M. C. Holthausen, A. Fiedler, H. Schwarz, W. Koch, *J. Phys. Chem.* **1996**, *100*, 6236.
[10] M. C. Holthausen, W. Koch, *J. Am. Chem. Soc.* **1996**, *118*, 9932.
[11] M. C. Holthausen, W. Koch, *Helv. Chim. Acta* **1996**, *79*, 1939.
[12] P. E. M. Siegbahn, M. R. A. Blomberg, *J. Am. Chem. Soc.* **1992**, *114*, 10548.
[13] A. M. C. Wittborn, M. Costas, M. R. A. Blomberg, P. E. M. Siegbahn, *J. Chem. Phys.* **1997**, *107*, 4318.
[14] J. K. Perry, PhD thesis, California Inst. of Technology, **1994**.
[15] M. C. Holthausen, A. Fiedler, H. Schwarz, W. Koch, *Angew. Chem.* **1995**, *107*, 2430; *Angew. Chem. Int. Ed. Engl.* **1995**, *34*, 2282.
[16] P. A. M. van Koppen, M. T. Bowers, E. R. Fisher, P. B. Armentrout, *J. Am. Chem. Soc.* **1994**, *116*, 3780.
[17] E. R. Fisher, L. S. Sunderlin, P. B. Armentrout, *J. Phys. Chem.* **1989**, *93*, 7375.
[18] P. A. M. van Koppen, P. R. Kemper, M. T. Bowers, *J. Am. Chem. Soc.* **1992**, *114*, 10941.
[19] P. A. M. van Koppen, J. Brodbelt-Lustig, M. T. Bowers, D. V. Dearden, J. L. Beauchamp, E. R. Fisher, P. B. Armentrout, *J. Am. Chem. Soc.* **1990**, *112*, 5663.
[20] D. B. Jacobson, B. S. Freiser, *J. Am. Chem. Soc.* **1983**, *105*, 5197.
[21] R. Georgiadis, E. R. Fisher, P. B. Armentrout, *J. Am. Chem. Soc.* **1989**, *111*, 4251.
[22] P. B. Armentrout, B. L. Tjelta, *Organometallics* **1997**, *16*, 5372–5374.
[23] S. D. Hanton, R. J. Noll, J. C. Weisshaar, *J. Chem. Phys.* **1992**, *96*, 5176.
[24] S. D. Hanton, R. J. Noll, J. C. Weisshaar, *J. Phys. Chem.* **1990**, *94*, 5655.
[25] R. H. Schultz, P. B. Armentrout, *J. Am. Chem. Soc.* **1991**, *113*, 729.
[26] R. J. Noll, PhD thesis, University of Wisconsin-Madison, **1994**.
[27] T. G. Dietz, M. A. Duncan, D. E. Powers, R. E. Smalley, *J. Chem. Phys.* **1981**, *74*, 6511.
[28] J. Sugar, C. Corliss, *J. Phys. Chem. Ref. Data* **1985**, *14*, Suppl. 2.
[29] R. H. Page, C. S. Gudeman, *J. Opt. Soc. Am.* **1990**, *B7*, 1761.
[30] W. C. Wiley, I. H. McLaren, *Rev. Sci. Instrum.* **1955**, *26*, 1150.
[31] R. J. Gallagher, PhD thesis, Yale University, **1972**.
[32] G. Cooper, Y. Zheng, G. R. Burton, C. E. Brion, *Rev. Sci. Instrum.* **1993**, *64*, 1140.
[33] W. W. Hunt, R. E. Huffman, K. E. McGee, *Rev. Sci. Instrum.* **1964**, *35*, 82.
[34] R. E. Ferguson, K. E. McCulloh, H. M. Rosenstock, *J. Chem. Phys.* **1965**, *42*, 100.
[35] D. L. Dugger, R. W. Kiser, *J. Chem. Phys.* **1967**, *47*, 5054.
[36] G. Gioumousis, D. P. Stevenson, *J. Chem. Phys.* **1958**, *29*, 294.
[37] C. L. Haynes, E. R. Fisher, P. B. Armentrout, *J. Phys. Chem.* **1996**, *100*, 18300.
[38] P. B. Armentrout, J. L. Beauchamp, *J. Am. Chem. Soc.* **1981**, *103*, 784.
[39] L. F. Halle, P. B. Armentrout, J. L. Beauchamp, *Organometallics* **1982**, *1*, 963.
[40] R. Houriet, L. F. Halle, J. L. Beauchamp, *Organometallics* **1983**, *2*, 1818.
[41] P. A. M. van Koppen, J. Brodbelt-Lustig, M. T. Bowers, D. V. Dearden, J. L. Beauchamp, E. R. Fisher, P. B. Armentrout, *J. Am. Chem. Soc.* **1991**, *113*, 2359.
[42] R. Tonkyn, M. Ronan, J. C. Weisshaar, *J. Phys. Chem.* **1988**, *92*, 92.
[43] M. A. Tolbert, J. L. Beauchamp, *J. Am. Chem. Soc.* **1986**, *108*, 7509.
[44] P. A. M. van Koppen, personal communication.
[45] M. C. Holthausen, T. Dargel, W. Koch, unpublished results.
[46] A. D. Becke, *J. Chem. Phys.* **1993**, *98*, 5648.
[47] P. J. Stevens, F. J. Devlin, C. F. Chabalowski, M. J. Frisch, *J. Phys. Chem.* **1994**, *98*, 11623.
[48] M. J. Frisch, G. W. Trucks, H. B. Schlegel, G. E. Scuseria, M. A. Robb, J. R. Cheeseman, V. G. Zakrzewski, J. A. Montgomery, R. E. Strat-

  0947-6539/00/0612-2244 $ 17.50+.50/0

mann, J. C. Burant, S. Dapprich, J. M. Millam, A. D. Daniels, K. N. Kudin, M. C. Strain, O. Farkas, J. Tomasi, V. Barone, M. Cossi, R. Cammi, B. Mennucci, C. Pomelli, C. Adamo, S. Clifford, J. Ochterski, G. A. Petersson, P. Y. Ayala, Q. Cui, K. Morokuma, D. K. Malick, A. D. Rabuck, K. Raghavachari, J. B. Foresman, J. Cioslowski, J. V. Ortiz, B. B. Stefanov, G. Liu, A. Liashenko, P. Piskorz, I. Komaromi, R. Gomperts, R. L. Martin, D. J. Fox, T. Keith, M. A. Al-Laham, C. Y. Peng, M. W. Nayakkara, C. Gonzalez, M. Challacombe, P. M. W. Gill, B. G. Johnson, W. Chen, M. W. Wong, J. L. Andres, M. Head-Gordon, E. S. Replogle, J. A. Pople, *Gaussian 98, Revision A.1*, Gaussian, Inc., Pittsburgh, PA, **1998**.

[49] A. J. H. Wachters, *J. Chem. Phys.* **1970**, *52*, 1033.

[50] P. J. Hay, W. R. Wadt, *J. Chem. Phys.* **1985**, *82*, 299.

[51] T. H. Dunning, P. J. Hay in *Modern Theoretical Chemistry* (Ed.: H. F. Schaefer), Plenum, New York, **1976**.

[52] P. J. Hay, *J. Chem. Phys.* **1977**, *66*, 4377.

[53] A. Ricca, C. W. Bauschlicher, *Chem. Phys. Lett.* **1995**, *245*, 150.

[54] K. Raghavachari, G. W. Trucks, *J. Chem. Phys.* **1989**, *91*, 1062.

[55] P. J. Robinson, K. A. Holbrook, *Unimolecular Reactions,* Wiley-Interscience, New York, **1972**.

[56] R. G. Gilbert, S. C. Smith, *Theory of Unimolecular and Recombination Reactions,* Blackwell Scientific Publications, Oxford, UK, **1990**.

[57] T. Baer, W. L. Hase, *Unimolecular Reaction Dynamics,* Oxford University Press, New York, **1996**.

[58] S. E. Stein, B. S. Ravinovitch, *J. Chem. Phys.* **1973**, *58*, 2438.

[59] T. Beyer, D. F. Swinehart, *Comm. Assoc. Comput. Machines* **1973**, *16*, 379.

[60] D. G. Fedorov, M. S. Gordon, unpublished results .

[61] P. B. Armentrout, Y.-M. Chen, *J. Am. Soc. Mass Spectrom.* **1999**, *10*, 821.

[62] M. Brookhart, M. L. H. Greem, *J. Organomet. Chem.* **1983**, *250*, 395.

[63] R. H. Grubbs, G. W. Coates, *Acc. Chem. Res.* **1996**, *29*, 85.

Received: December 21, 1999 [F2199]